articles

molecular pharmaceutics

Pulsed Ultrasound Enhances Nanoparticle Penetration into Breast Cancer Spheroids

Stephanie J. Grainger, Juliana Valencia Serna, Steffi Sunny, Yun Zhou, Cheri X. Deng, and Mohamed E. H. El-Sayed*

Department of Biomedical Engineering, University of Michigan, 1101 Beal Avenue, Ann Arbor, Michigan 48109, United States

Received August 23, 2010; Revised Manuscript Received October 18, 2010; Accepted October 19, 2010

Abstract: Effective treatment of solid tumors requires homogeneous distribution of anticancer drugs within the entire tumor volume to deliver lethal concentrations to resistant cancer cells and tumor-initiating cancer stem cells. However, penetration of small molecular weight chemotherapeutic agents and drug-loaded polymeric and lipid particles into the hypoxic and necrotic regions of solid tumors remains a significant challenge. This article reports the results of pulsed ultrasound enhanced penetration of nanosized fluorescent particles into MCF-7 breast cancer spheroids (300−350 μm diameter) as a function of particle size and charge. With pulsed ultrasound application in the presence of microbubbles, small (20 nm) particles achieve 6−20-fold higher penetration and concentration in the spheroid's core compared to those not exposed to ultrasound. Increase in particle size to 40 and 100 nm results in their effective penetration into the spheroid's core to 9- and 3-fold, respectively. In addition, anionic carboxylate particles achieved higher penetration (2.3-, 3.7-, and 4.7-fold) into the core of MCF-7 breast cancer spheroids compared to neutral (2.2-, 1.9-, and 2.4-fold) and cationic particles (1.5-, 1.4-, and 1.9-fold) upon US exposure for 30, 60, and 90 s under the same experimental conditions. These results demonstrate the feasibility of utilizing pulsed ultrasound to increase the penetration of nanosized particles into MCF-7 spheroids mimicking tumor tissue. The effects of particle properties on the penetration enhancement were also illustrated.

Keywords: Ultrasound; microbubbles; nanoparticles; spheroids; drug delivery; fluorescence microscopy

Introduction

Solid tumors are characterized by a unique pathological microenvironment that incorporates rapidly proliferating cancer cells,[1] a poorly organized vascular network with irregular blood flow,[2−6] and an impaired lymphatic drainage system.[7] Earlier studies confirmed the leakiness of tumor vasculature, which allows plasma proteins and other macromolecules to diffuse from the systemic blood circulation into the interstitial tissue.[8] This high vascular permeability is attributed to poor endothelial cell alignment, formation of wide fenestrations,[9−11] and overexpression of vascular permeability factors such as nitric oxide, bradykinin, and prostaglandins.[12−16] This high permeability of tumor vasculature has been exploited to target anticancer drugs to cancer cells using polymeric and lipid carriers.[17−21] However, penetration of both small molecular weight chemo-

* Corresponding author. Mailing address: University of Michigan, Department of Biomedical Engineering, 1101 Beal Avenue, Lurie Biomedical Engineering Building, Room 2150, Ann Arbor, MI 48109. Phone: +1 (734) 615-9404. Fax: +1 (734) 647-4834. E-mail: melsayed@umich.edu. Web: www.bme.umich.edu/centlab.php.

(1) Denekamp, J.; Hobson, B. Endothelial-cell proliferation in experimental tumours. *Br. J. Cancer* **1982**, *46*, 711–720.

(2) Less, J. L.; Skalak, E. M.; Sevick, E. M.; Jain, R. K. Micrvascular architecture in a mammary carcinoma: branching patterns and vessel dimensions. *Cancer Res.* **1991**, *51*, 265–273.

(3) Intaglietta, M.; Myers, R. R.; Gross, J. F.; Reinhold, H. S. Dynamics of microvascular flow in implanted mouse mammary tumours. *Bibl. Anat.* **1977**, *15* (1), 273–276.

(4) Chaplin, D. J.; Olive, P. L.; Durand, R. E. Intermittent blood flow in a murine tumour: Radiobiological effects. *Cancer Res.* **1987**, *47*, 597–601.

10.1021/mp100280b
Published on Web 10/19/2010

therapeutics and drug-loaded particulate carriers deep into tumor tissue proved to be a significant challenge.[22−25]

High vascular permeability coupled with the impaired lymphatic drainage increase a tumor's interstitial fluid pressure, which hinders the transport of anticancer drugs from the systemic circulation into tumor stroma.[26−28] In addition, high collagen content in a tumor's extracellular matrix and its organization into a thick fibrous network particularly in poorly vascularized and hypoxic regions increase tissue stiffness, providing an additional physical barrier that further limits the penetration of anticancer drugs.[29−32] Failure of current anticancer drugs to achieve efficient penetration and uninform distribution in tumor tissue limits their ability to reach tumor stem cells sequestered in the tumor's necrotic core at sufficient concentrations to trigger their death (Figure 1).[33] Consequently, current anticancer treatments are unable to completely eradicate viable cancer cells and often lead to the development of chemo- and radiation-resistant cells that initiate tumor recurrence.[24,34−36]

Jain and co-workers used an antibody targeted to the vascular endothelial growth factor receptor to inhibit angio-

(5) Chaplin, D. J.; Trotter, M. J.; Durand, R. E.; Olive, P. L.; Minchinton, A. I. Evidence for intermittent radiobiological hypoxia in experimental tumour systems. *Biomed. Biochim. Acta* **1989**, *48*, 255–259.

(6) Dewhirst, M. W.; Braun, R. D.; Lanzen, J. L. Temporal changes in PO_2 of R3230AC tumors in Fischer-344 rats. *Int. J. Radiat. Oncol. Biol. Phys.* **1998**, *42*, 723–726.

(7) Leu, A. J.; Berk, D. A.; Lymboussaki, A.; Alitalo, K.; Jain, R. K. Absence of functional lymphatics within a murine sarcoma: A molecular and functional evaluation. *Cancer Res.* **2000**, *60* (16), 4324–4327.

(8) Jain, R. K.; Munn, L. L.; Fukumura, D. Dissecting tumour pathophysiology using intravital microscopy. *Nat. Rev. Cancer* **2002**, *2* (4), 266–276.

(9) Skinner, S.; Tutton, P.; O'Brien, P. E. Microvascular architecture of experimental colon tumors in the rat. *Cancer Res.* **1990**, *50*, 2411–2417.

(10) Hashizume, H.; Baluk, P.; Morikawa, S.; McLean, J. W.; Thurston, G.; Roberge, S.; Jain, R. K.; McDonald, D. M. Openings between defective endothelial cells explain tumor vessel leakiness. *Am. J. Pathol.* **2000**, *56*, 1363–1380.

(11) Yuan, F.; Dellian, M.; Fukumura, D.; Leunig, M.; Berk, D. A.; Torchilin, V. P.; Jain, R. K. Vascular permeability in a human tumor xenograft: Molecular size dependence and cutoff size. *Cancer Res.* **1995**, *55*, 3752–3756.

(12) Senger, D. R.; Galli, S. J.; Dvorak, A.; Perruzzi, C.; Harvey, V.; Dvorak, F. Tumor cells secrete a vascular permeability factor that promotes accumulation of ascites fluid. *Science* **1983**, *219*, 983–985.

(13) Maeda, H.; Noguchi, Y.; Sato, K.; Akaike, T. Enhanced vascular permeability in solid tumor is mediated by nitric oxide and inhibited by both new nitric oxide scavenger and nitric oxide synthase inhibitor. *Jpn. J. Cancer Res.* **1994**, *85*, 331–334.

(14) Maeda, H.; Akaike, T.; Wu, J.; Noguchi, Y.; Sakata, Y. Bradykinin and nitric oxide in infectious disease and cancer. *Immunopharmacology* **1996**, *33*, 222–230.

(15) Wu, J.; Akaike, T.; Maeda, H. Modulation of enhanced vascular permeability in tumors by a bradykinin antagonist, a cyclooxygenase inhibitor, and a nitric oxide scavenger. *Cancer Res.* **1998**, *58*, 159–165.

(16) Wu, J.; Akaike, T.; Hyashida, K.; Okamoto, T.; Okuyama, A.; Maeda, H. Enhanced vascular permeability in solid tumor involving peroxynitite and matrix metalloproteinases. *Jpn. J. Cancer Res.* **2001**, *92*, 439–451.

(17) Duncan, R. Polymer conjugates for tumour targeting and intracytoplasmic delivery. The EPR effect as a common gateway. *Pharm. Sci. Technol. Today* **1999**, *2* (11), 441–449.

(18) Greish, K. Enhanced permeability and retention (EPR) effect for anticancer nanomedicine drug targeting. *Methods Mol. Biol.* **2010**, *624*, 25–37.

(19) Maeda, H. The enhanced permeability and retention (EPR) effect in tumor vasculature: The key role of tumor-selective macromolecular drug targeting. *Adv. Enzyme Regul.* **2001**, *41*, 189–207.

(20) Maeda, H.; Matsumura, Y. Tumoritropic and lymphotropic principles of macromolecular drugs. *Crit. Rev. Ther. Drug Carrier Syst.* **1989**, *6* (3), 193–210.

(21) Maeda, H.; Oda, T.; Matsumura, Y.; Kimura, M. Improvement of pharmacological properties of protein drugs by tailoring with synthetic polymers. *J. Bioact. Compat. Polym.* **1988**, *3*, 27–43.

(22) Primeau, A. J.; Rendon, A.; Hedley, D.; Lilge, L.; Tannock, I. F. The distribution of the anticancer drug doxorubicin in relation to blood vessels in solid tumors. *Clin. Cancer Res.* **2005**, *11* (24), 8782–8788.

(23) Grantab, R.; Sivananthan, S.; Tannock, I. F. The penetration of anticancer drugs through tumor tissue as a function of cellular adhesion and packing density of tumor cells. *Cancer Res.* **2006**, *66* (2), 1033–1039.

(24) Kyle, A. H.; Huxham, L. A.; M.Yeoman, D.; Minchinton, A. I. Limited tissue penetration of taxanes: A mechanism for resistance in solid tumors. *Clin. Cancer Res.* **2007**, *13* (9), 2804–2810.

(25) Minchinton, A. I.; Tannock, I. F. Drug penetration in solid tumours. *Nat. Rev. Cancer* **2006**, *6*, 583–592.

(26) Boucher, Y.; Brekken, C.; Netti, P. A.; Baxter, L. T.; Jain, R. K. Intratumoral infusion of fluid: estimation of hydraulic conductivity and implications for the delivery of therapeutic agents. *Br. J. Cancer* **1998**, *78* (11), 1442–1448.

(27) Hassid, Y.; Eyal, E.; Margalit, R.; Furman-Haran, E.; Degani, H. Non-invasive imaging of barriers to drug delivery in tumors. *Microvasc. Res.* **2008**, *76* (2), 94–103.

(28) Heldin, C. H.; Rubin, K.; Pietras, K.; Ostman, A. High interstitial fluid pressure - An obstacle in cancer therapy. *Nat. Rev. Cancer* **2004**, *4* (10), 806–813.

(29) Netti, P. A.; Berk, D. A.; Swartz, M. A.; Grodzinsky, A. J.; Jain, R. K. Role of extracellular matrix assembly in interstitial transport in solid tumors. *Cancer Res.* **2000**, *60* (9), 2497–2503.

(30) Davies, C. d. L.; Berk, D. A.; Pluen, A.; Jain, R. K. Comparison of IgG diffusion and extracellular matrix composition in rhabdomyosarcomas grown in mice versus *in vitro* as spheroids reveals the role of host stromal cells. *Br. J. Cancer* **2002**, *86*, 1639–1644.

(31) Brown, E.; McKee, T.; di Tomaso, E.; Pluen, A.; Seed, B.; Boucher, E.; Jain, R. K. Dynamic imaging of collagen and its modulation in tumors in vivo using second-harmonic generation. *Nat. Med.* **2003**, *9*, 796–800.

(32) Choi, J.; Credit, K.; Henderson, K.; Deverkadra, R.; He, Z.; Wiig, H.; Vanpelt, H.; Flessner, M. F. Intraperitoneal immunotherapy for metastatic ovarian carcinoma: Resistance of intratumoral collagen to antibody penetration. *Clin. Cancer Res.* **2006**, *12*, 1906–1912.

(33) Dean, M.; Fojo, T.; Bates, S. Tumor stem cells and drug resistance. *Nat. Rev. Cancer* **2005**, *5* (4), 275–284.

(34) Sutherland, R. M.; Eddy, H. A.; Bareham, B.; Reich, K.; Vanantwerp, D. Resistance to Adriamycin in multicellular spheroids. *Int. J. Radiat. Oncol. Biol. Phys.* **1979**, *5*, 1225–1230.

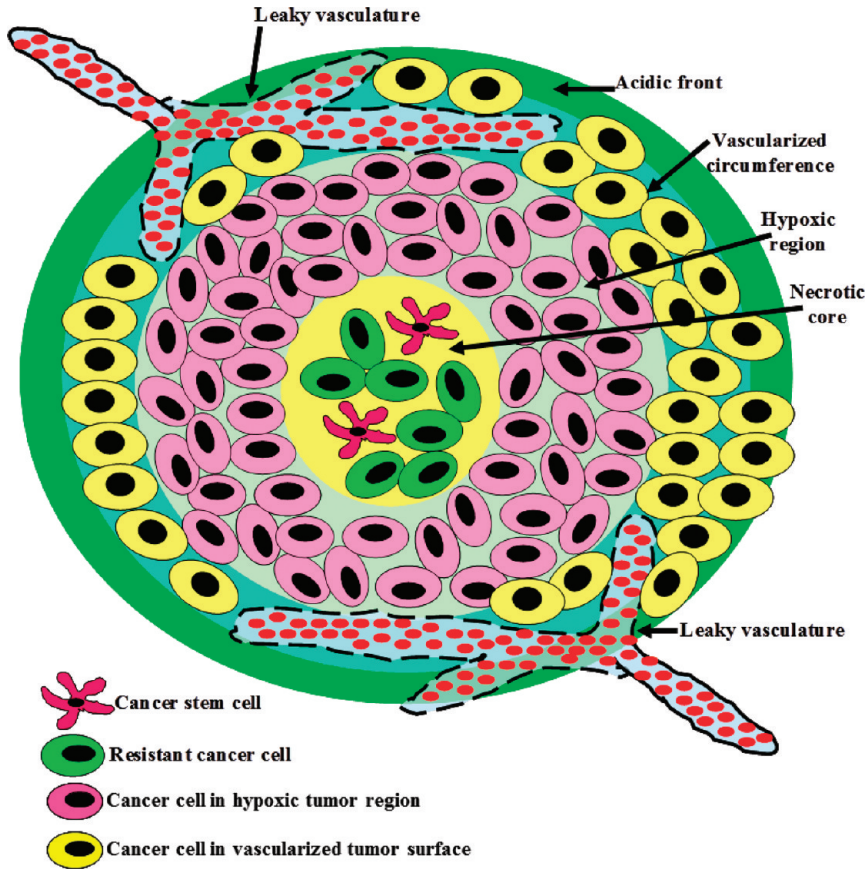

Figure 1. A schematic drawing showing the organization of solid tumors with the characteristic acidic front, vascularized circumference, hypoxic region, and necrotic core. Cancer stem cells and resistant cancer cells are typically sequestered in a tumor's hypoxic and necrotic regions.

genesis, "normalize" tumor vasculature, reduce the interstitial fluid pressure, and consequently enhance the penetration of anticancer drugs into tumor tissue.[37] This strategy proved effective in pruning immature blood vessels, improving the integrity and function of the remaining vasculature by enhancing the perivascular cell and basement membrane coverage, and increasing the penetration of fluorescent molecules into the interstitial tissue.[37] However, recent studies showed that normalizing the vascular bed and reducing the interstitial fluid pressure using angiogenesis inhibitors were not sufficient to increase the penetration of drug-loaded liposomes into tumor tissue due to diminished permeability of a tumor's vasculature.[38]

Alternatively, several groups relied on direct injection of collagenase and hyaluronidase enzymes into tumor tissue to degrade the extracellular matrix and increase the penetration of oncolytic viruses, antibodies, and therapeutic nanoparticles into the interstitial tissue.[39−44] Pun and co-workers showed that collagenase-coated particles exhibit higher penetration into cervical cancer spheroids.[45] However, the therapeutic utility of these protease enzymes relies on the ability to design nanocarriers that can deliver these enzymes exclusively to the tumor tissue and achieve site-specific degradation of the extracellular matrix to enhance the penetration of the loaded therapeutic cargo. Failure to guide these enzyme-loaded particles to the tumor tissue will result in nonspecific degradation of connective tissue in healthy organs, particularly the liver, lungs, kidneys and spleen, which are known to scavenge particulate carriers from the system circulation leading to significant toxicities.[46−48]

On the other hand, with the ability to noninvasively target a specific location *in vivo* (e.g., tumor lesions) without increasing systemic exposure, ultrasound (US) techniques have been

(35) Tannock, I. F.; Lee, C. M.; Tunggal, J. K.; Cowan, D. S.; Egorin, M. J. Limited penetration of anticancer drugs through tumor tissue: a potential cause of resistance of solid tumors to chemotherapy. *Clin. Cancer Res.* **2002**, *8*, 878–884.

(36) Olive, P. L.; Durand, R. E. Drug and radiation resistance in spheroids: cell contact and kinetics. *Cancer Metastasis Rev.* **1994**, *13*, 121–138.

(37) Tong, R. T.; Boucher, Y.; Kozin, S. V.; Winkler, F.; Hicklin, D. J.; Jain, R. K. Vascular normalization by vascular endothelial growth factor receptor 2 blockade induces a pressure gradient across the vasculature and improves drug penetration in tumors. *Cancer Res.* **2004**, *64* (11), 3731–3736.

(38) Tailor, T. D.; Hanna, G.; Yarmolenko, P. S.; Dreher, M. R.; Betof, A. S.; Nixon, A. B.; Spasojevic, I.; Dewhirst, M. W. Effect of pazopanib on tumor microenvironment and liposome delivery. *Mol. Cancer Ther.* **2010**, *9* (6), 1798–1808.

(39) Eikenes, L.; Bruland, O. S.; Brekken, C.; Davies, C. L. Collagenase increases the transcapillary pressure gradient and improves the uptake and distribution of monoclonal antibodies in human osteosarcoma xenografts. *Cancer Res.* **2004**, *64*, 4768–4773.

exploited as a novel strategy utilizing physical energy to enhance tumor-specific drug delivery.[49−53] For example, US application has been shown to increase the effectiveness of adriamycin against ovarian cancer in nude tumor-bearing mice[54] and enhance the uptake of radiolabeled monoclonal antibody to human epidermoid tumor in nude mice.[55]

The US field generates rapid cyclic changes in pressure and fluid flow, which can result in biomechanical effects such as shear stress on cells and biological systems. In particular, due to the efficient interaction of US with gaseous bubbles, microbubble-enhanced US exposures have been used to produce significant mechanical impacts such as high shear stress,[56−58] microstreaming,[59,60] shock waves,[61−63] and other mechanical forces[62,63] on nearby cells and tissue via the rapid volume changes and violent collapse (cavitation) of the microbubbles.[64,65] The mechanical effects produced by acoustic cavitation have been exploited for enhancing direct intracellular drug delivery via sonoporation (membrane disruption caused by ultrasound)[66−68] and delivery across endothelial barriers.[69,70] For example, US has been shown to enhance radionuclide uptake in pancreatic tumor cells *in*

(40) Eikenes, L.; Tari, M.; Tufto, I.; Bruland, O. S.; Davies, C. L. Hyaluronidase induces a transcapillary pressure gradient and improves the distribution and uptake of liposomal doxorubicin (Caelyx (TM)) in human osteosarcoma xenografts. *Br. J. Cancer* **2005**, *93*, 81–88.

(41) McKee, T. D.; Grandi, P.; Mok, W.; Alexandrakis, G.; Insin, N.; Zimmer, J. P.; Bawendi, M. G.; Boucher, Y.; Breakefield, X. O.; Jain, R. K. Degradation of fibrillar collagen in a human melanoma xenograft improves the efficacy of an oncolytic herpes simplex virus vector. *Cancer Res.* **2006**, *66*, 2509–2513.

(42) Choi, I.-K.; Lee, Y.-S.; Yoo, J. Y.; Yoon, A.-R.; Kim, H.; Kim, D.-S.; Seidler, D. G.; Kim, J.-H.; Yun, C.-O. Effect of decorin on overcoming the extracellular matrix barrier for oncolytic virotherapy. *Gene Ther.* **2010**, *17*, 190–201.

(43) Eikenes, L.; Tufto, I.; Schnell, E. A.; Bjorkoy, A.; Davies, C. d. L. Effect of collagenase and hylauronidase on free and anomalous diffusion in multicellular spheroids and xenografts. *Anticancer Res.* **2010**, *30* (2), 359–368.

(44) Kuriyama, N.; Kuriyama, H.; Julin, C. M.; Lamborn, K. R.; Israel, M. A. Protease pretreatment increases the efficacy of adenovirus-mediated gene therapy for the treatment of an experimental glioblastoma model. *Cancer Res.* **2001**, *61*, 1805–1809.

(45) Goodman, T. T.; Olive, P. L.; Pun, S. H. Increased nanoparticle penetration in collagenase treated multicellular spheroids. *Int. J. Nanomed.* **2007**, *2* (2), 265–274.

(46) Decuzzi, P.; Godin, B.; Tanaka, T.; Lee, S. Y.; Chiappini, C.; Liu, X.; Ferrari, M. Size and shape effects in the biodistribution of intravascularly injected particles. *J. Controlled Release* **2010**, *141* (3), 320–327.

(47) Semmler-Behnke, M.; Kreyling, W. G.; Lipka, J.; Fertsch, S.; Wenk, A.; Takenaka, S.; Schmid, G.; Brandau, W. Biodistribution of 1.4-and 18-nm Gold Particles in Rats. *Small* **2008**, *4* (12), 2108–2111.

(48) Sheng, Y.; Yuan, Y.; Liu, C. S.; Tao, X. Y.; Shan, X. Q.; Xu, F. *In vitro* macrophage uptake and *in vivo* biodistribution of PLA-PEG nanoparticles loaded with hemoglobin as blood substitutes: effect of PEG content. *J. Mater. Sci.: Mater. Med.* **2009**, *20* (9), 1881–1891.

(49) Frenkel, V. Ultrasound mediated delivery of drugs and genes to solid tumors. *Adv. Drug Delivery Rev.* **2008**, *60* (10), 1193–1208.

(50) O'Neill, B. E.; Vo, H.; Angstadt, M.; Li, K. P.; Quinn, T.; Frenkel, V. Pulsed high intensity focused ultrasound mediated nanoparticle delivery: mechanisms and efficacy in murine muscle. *Ultrasound Med. Biol.* **2009**, *35* (3), 416–424.

(51) Pitt, W. G.; Husseini, G. A.; Staples, B. J. Ultrasonic drug delivery—a general review. *Expert Opin. Drug Delivery* **2004**, *1* (1), 37–56.

(52) Staples, B. J.; Roeder, B. L.; Husseini, G. A.; Badamjav, O.; Schaalje, G. B.; Pitt, W. G. Role of frequency and mechanical index in ultrasonic-enhanced chemotherapy in rats. *Cancer Chemother. Pharmacol.* **2009**, *64* (3), 593–600.

(53) Yuh, E. L.; Shulman, S. G.; Mehta, S. A.; Xie, J.; Chen, L.; Frenkel, V.; Bednarski, M. D.; Li, K. C. Delivery of systemic chemotherapeutic agent to tumors by using focused ultrasound: study in a murine model. *Radiology* **2005**, *234* (2), 431–437.

(54) Yu, T.; Huang, X.; Hu, K.; Bai, J.; Wang, Z. Treatment of transplanted adriamycin-resistant ovarian cancers in mice by combination of adriamycin and ultrasound exposure. *Ultrason. Sonochem.* **2004**, *11*, 287–291.

(55) Khaibullina, A.; Jang, B. S.; Sun, H.; Le, N.; Yu, S.; Frenkel, V.; Carrasquillo, J. A.; Pastan, I.; Li, K. C.; Paik, C. H. Pulsed high-intensity focused ultrasound enhances uptake of radiolabeled monoclonal antibody to human epidermoid tumor in nude mice. *J. Nucl. Med.* **2008**, *49* (2), 295–302.

(56) Wu, J. Shear stress in cells generated by ultrasound. *Prog. Biophys. Mol. Biol.* **2007**, *93*, 363–373.

(57) Collis, J.; Manasseha, R.; Liovic, P.; Tho, P.; Ooi, A.; Petkovic-Duran, K.; Zhu, Y. Cavitation microstreaming and stress fields created by microbubbles. *Ultrasonics* , *50* (2), 273–279.

(58) VanBavel, E. Effects of shear stress on endothelial cells: possible relevance for ultrasound applications. *Prog. Biophys. Mol. Biol.* **2007**, *93*, 374–383.

(59) Collis, J.; Manasseh, R.; Liovic, P.; Tho, P.; Ooi, A.; Petkovic-Duran, K.; Zhu, Y. G. Cavitation microstreaming and stress fields created by microbubbles. *Ultrasonics* **2010**, *50* (2), 273–279.

(60) van Wamel, A.; Kooiman, K.; Harteveld, M.; Emmer, M.; ten Cate, F. J.; Versluis, M.; de Jong, N. Vibrating microbubbles poking individual cells: Drug transfer into cells via sonoporation. *J. Controlled Release* **2006**, *112* (2), 149–155.

(61) Postema, M.; Wamel, A. v.; Lancee, C. T.; Jong, N. d. Ultrasound-induced encapsulated microbubble phenomena. *Ultrasound Med. Biol.* **2004**, *30*, 827–840.

(62) Prentice, P.; Cuschieri, A.; Dholakia, K.; Prausnitz, M.; Campbell, P. Membrane disruption by optically controlled microbubble cavitation. *Nat. Phys.* **2005**, *1*, 107–110.

(63) Ohl, C. D.; Arora, M.; Ikink, R.; de Jong, N.; Versluis, M.; Delius, M.; Lohse, D. Sonoporation from jetting cavitation bubbles. *Biophys. J.* **2006**, *91*, 4285–4295.

(64) Lindner, J. R. Microbubbles in medical imaging: current applications and future directions. *Nat. Rev. Drug Discovery* **2004**, *3*, 527–532.

(65) Pecha, R.; Gompf, B. Microimplosions: Cavitation collapse and shock wave emission on a nanosecond time scale. *Phys. Rev. Lett.* **2000**, *84* (6), 1328–1330.

(66) Guzman, H.; McNamara, A. J.; Nguyen, D. X.; Prausnitz, M. R. Bioeffects caused by changes in acoustic cavitation bubble density and cell concentration: a unified explanation based on cell-to-bubble ratio and blast radius. *Ultrasound Med. Biol.* **2003**, *29*, 1211–1222.

(67) Zhou, Y.; Shi, J.; Cui, J.; Deng, C. X. Effects of extracellular calcium on cell membrane resealing in sonoporation. *J. Controlled Release* **2008**, *126*, 34–43.

vitro.[71] While various mechanisms have been investigated for US enhanced drug delivery without specific use of microbubbles,[50,52,72,73] the use of microbubble facilitated delivery is of great interest because of the advantages and potential of combining the imaging and therapeutic capabilities using microbubble-based carriers for image-guided therapy.[74−77] However, despite many encouraging results, no detailed information or mechanisms have been reported describing how various factors influence the penetration of nanoparticles into solid tumors in the presence of microbubbles and how to achieve optimal delivery outcome in solid tumors using ultrasonic techniques.

In this study, we investigate the effects of pulsed US in the presence of microubbles on the penetration and retention of model fluorescent nanoparticles into breast cancer spheroids as a 3D *in vitro* tumor model (Figure 2). With the controlled experimental model and conditions in this study, the effects of pulsed US duty cycle (DC) (10−50% duty cycle) and exposure time (30, 60, 90 s), particle size (20, 40, 100 nm), surface chemistry, and charge (COOH/−, NH_2/+, neutral) were examined to illustrate the interplay among the particle's physicochemical properties, the applied US, and the depth of penetration into breast cancer spheroids, which can provide insights for the design of new strategies for US-assisted delivery of therapeutic and diagnostic agents into solid tumors.

(68) Deng, C.; Sieling, F.; Pan, H.; Cui, J. Ultrasound-induced cell membrane porosity. *Ultrasound Med. Biol.* **2004**, *30* (4), 519–526.
(69) Price, R. J.; Skyba, D. M.; Kaul, S.; Skalak, T. C. Delivery of colloidal particles and red blood cells to tissue through microvessel ruptures created by targeted microbubble destruction with ultrasound. *Circulation* **1998**, *98*, 1264–1267.
(70) Park, J.; Fan, Z.; Kumon, R. E.; El-Sayed, M. E. H.; Deng, C. X. Modulation of intracellular calcium concentration in brain microvascular endothelial cells *in vitro* by acoustic cavitation. *Ultrasound Med. Biol.* **2010**, *36* (7), 1176–1187.
(71) Wamel, A. v.; Bouakaz, A.; Bernard, B.; Cate, F. t.; Jong, N. d. Radionuclide tumour therapy with ultrasound contrast microbubbles. *Ultrasonics* **2004**, *42*, 903–906.
(72) Hancock, H. A.; Smith, L. H.; Cuesta, J.; Durrani, A. K.; Angstadt, M.; Palmeri, M. L.; Kimmel, E.; Frenkel, V. Investigations into pulsed high-intensity focused ultrasound-enhanced delivery: preliminary evidence for a novel mechanism. *Ultrasound Med. Biol.* **2009**, *35* (10), 1722–1736.
(73) Husseini, G. A.; Pitt, W. G. Micelles and nanoparticles for ultrasonic drug and gene delivery. *Adv. Drug Delivery Rev.* **2008**, *60* (10), 1137–1152.
(74) Ferrara, K.; Pollard, R.; Borden, M. Ultrasound microbubble contrast agents: Fundamentals and application to gene and drug delivery. *Annu. Rev. Biomed. Eng.* **2007**, *9*, 415–447.
(75) Ferrara, K. W. Driving delivery vehicles with ultrasound. *Adv. Drug Delivery Rev.* **2008**, *60* (10), 1097–1102.
(76) Ferrara, K. W.; Borden, M. A.; Zhang, H. Lipid-shelled vehicles: engineering for ultrasound molecular imaging and drug delivery. *Acc. Chem. Res.* **2009**, *42* (7), 881–892.
(77) Qin, S.; Caskey, C. F.; Ferrara, K. W. Ultrasound contrast microbubbles in imaging and therapy: physical principles and engineering. *Phys. Med. Biol.* **2009**, *54* (6), R27–57.

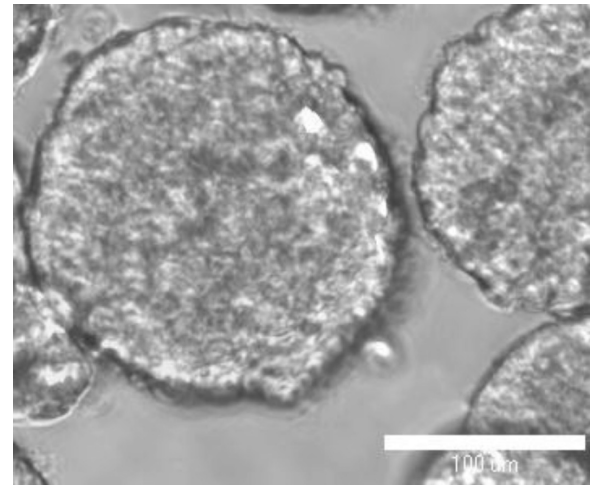

Figure 2. A representative phase contrast image of MCF-7 breast cancer spheroids suspended in PBS.

Materials and Methods

Cancer Cells and Fluorescent Nanoparticles. MCF-7 breast cancer cells were a generous gift from Dr. Sofia Merajver of the University of Michigan. MEM, fetal bovine serum, sodium pyruvate, bovine insulin, and 0.25% trypsin/EDTA solutions were purchased from Invitrogen Corporation (Carlsbad, CA). Fluorescein isothiocyanate (FITC)-loaded polystyrene particles ($\lambda_{ex/em}$ 480/515) with carboxylate surface groups (sizes 20, 40, and 100 nm) were also purchased from Invitrogen Corporation (Carlsbad, CA). CdSe quantum dots ($\lambda_{ex/em}$ 350/490) with either nonfunctionalized or amine-functionalized surfaces (size 20 nm) were purchased from eBioscience Inc. (San Diego, CA).

Culture of MCF-7 Cells and Formation of Breast Cancer Spheroids. MCF-7 breast cancer cells were cultured in MEM medium supplemented with 10% FBS, antibiotic/antimycotic solution, sodium pyruvate, and bovine insulin while changing the culture medium every 48 h following American Type Culture Collection established protocols. To initiate spheroid formation, agarose beads with an average diameter of 5−8 μm were prepared using 4% w/v agarose in phosphate buffered saline (PBS) solution and suspended in MEM culture medium supplemented with 10 mM glucose solution while stirring for eight hours. MCF-7 cells were trypsinized, and 10^9 cells were added to the bead solution and allowed to incubate for 1 h on an orbital shaker rotating at 100 rpm. This cell suspension was mixed with 150 mL of MEM culture medium supplemented with 10 mM glucose and pre-equilibrated with CO_2 in a 250 mL spinner flask (Bellco Glass, Vineland, NJ) and incubated at 37 °C, 5% CO_2, and 95% relative humidity while spinning at 150 rpm. The culture medium was replaced every eight hours for the first day followed by a daily medium change. The culture medium was sampled on a daily basis to visualize and measure the size of the growing spheroids using a Nikon EZ-C1 3.50 confocal microscope (Nikon Instruments Inc., Melville, NY) equipped with MetaMorph 7.5 software (Molecular Devices Inc., Sunnyvale, CA) until the spheroids

reached the desired size, 300−350 μm. MCF-7 spheroids (diameter = 300−350 μm) were stained using a 5 μM solution of Cell Tracker Red CMTPX dye (Molecular Probes Inc., Eugene, OR) to allow visualization and definition of spheroid boundaries by microscopic examination.

Microbubbles and US Application. Approximately 1000 stained spheroids were suspended in 1 mL of PBS (pH 7.4) and mixed with 3.64×10^{13} fluorescent particles and 50 μL of Optison microbubbles (GE Healthcare Biosciences, Pittsburgh, PA) in one of the wells in a 24-well plate to be exposed to pulsed US. Optison microbubbles, which are composed of octafluoropropane gas encapsulated by an albumin shell to form bubbles with an average diameter of ~3 μm, were added to the spheroid solution to enhance the US-induced mechanical effects. An unfocused circular planar piezoelectric US transducer (Piezo Technologies, Indianapolis, IN) with a center frequency of 1 MHz, driven by a waveform generator (model 33250A, Agilent Technologies, Palo Alto, CA), and a 75 W power amplifier (model 75A250, Amplifier Research, Souderton, PA) was used to generate the pulsed US at acoustic pressure amplitude of 0.5 MPa and pulse repetition frequency (PRF) of 10 Hz with various DC (10−50%) and exposure times (10−90 s). The US transducer was submerged in water in a water tank facing upward aiming at the well that housed the spheroids. The positioning of the 24-well plate was controlled by a customized 3D positioning system (Velmex Inc., Bloomfield, NY) and placed 3 cm above the US transducer. Only the bottom surface of the plate was submerged in water for acoustic coupling without contaminating the sample in the well of the plate. The acoustic pressure of the US pulses was measured using a needle hydrophone with an active element of 40 μm (Precision Acoustics HPM04/1, Dorset, U.K.) placed inside the well of the plate with the same configuration for the experiments. The effects of reflection and attenuation by the polyethylene derivative (~1 mm) plate bottom were measured to result in 10−15% reduction on the pressure amplitude.

Measurement of Particle Penetration into MCF-7 Spheroids. After US application at a given exposure condition, the spheroid solution was transferred to a microfuge tube, kept at room temperature for 10 min to allow the spheroids to settle down before removing the PBS supernatant, and suspending the spheroids in serum-free culture medium for microscopic examination. Spheroids were visualized using a Nikon EZ-C1 3.50 confocal microscope (Nikon Instruments Inc., Melville, NY) equipped with red ($\lambda_{ex/em} = \lambda_{577/602}$) and green ($\lambda_{ex/em} = \lambda_{488/518}$) filters. Several images were captured 1 μm apart along the vertical z-axis of each spheroid in the examination field to systematically show the penetration depth of different fluorescent particles (green) into the spheroids matrix (red) generating z-stacks for each experimental condition including the control group (i.e., spheroids mixed with the fluorescent particles and Optison microspheres but not exposed to US). Using MetaMorph 7.5, each cross section along the z-stack of each spheroid was divided equally into four concentric rings along the spheroid's radius (r) with the spheroid's surface and core designated as 1.00r and 0.25r, respectively (Figure 3). Forty equally spaced radii were used to measure the intensity of red and green fluorescence in each image and record these values based on the spatial distribution in the four predesignated rings (Figure 3). MatLab 7.0 (MathWorks Inc., Natick, MA) was used to compute the green fluorescence intensity and determine the localization of the fluorescent particles along the spheroid radius (red fluorescence) for each of the examined spheroids. Each experimental condition was evaluated in three independent experiments using triplicates in each experiment, and this data was analyzed to generate the reported penetration profiles.

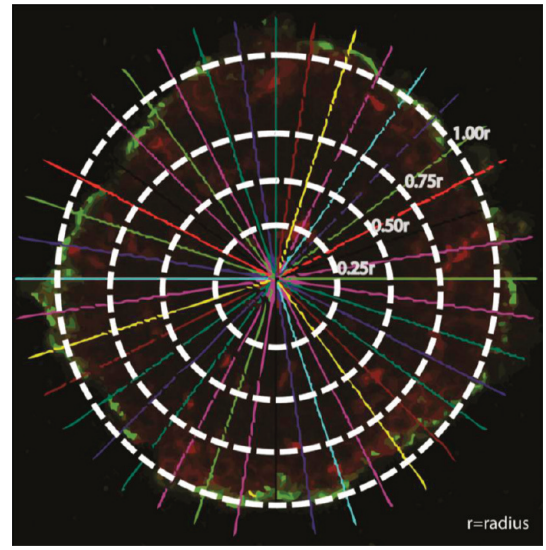

Figure 3. Image of an optical section along the z-axis of a breast cancer spheroid stained with Cell Tracker Red Dye and incubated with fluorescent nanoparticles (green color). The image shows four concentric rings representing 0.25r, 0.5r, 0.75r, and 1.00r where r is the spheroid's radius. The 40 lines originating from the spheroid's center pointing toward the spheroid's surface were used to divide the image into equal sections to measure the fluorescence intensity (red and green) along the spheroid's radius (r) to quantitatively measure the depth of penetration of fluorescent nanoparticles (green) into the spheroid's core.

Results

Following our protocol, MCF-7 cells formed large (>300 μm) viable spheroids within 5−6 days in culture, which were used in this experimental study (Figure 2). The effect of US exposures (DC and exposure duration) on the penetration of FITC-loaded polystyrene particles with carboxylic acid (COOH) surface groups into MCF-7 spheroids was examined as a function of particle size (20, 40, and 100 nm). We also evaluated the effect of surface chemistry and charge (COOH/anionic, NH_2/cationic, and neutral) on the penetration of 20 nm particles into MCF-7 spheroids at similar US duty cycle (10% DC) and exposure time. The fluorescence intensity in

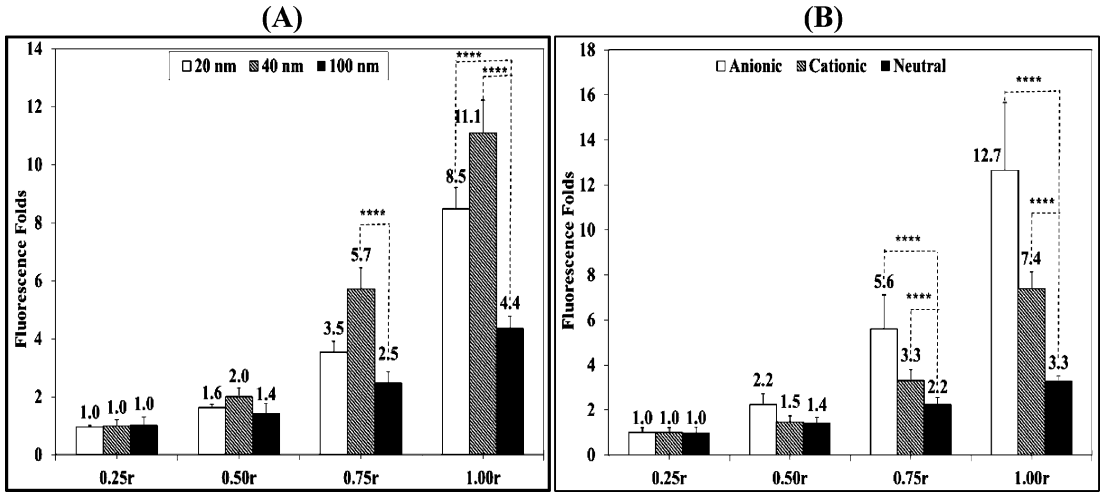

Figure 4. Change in fluorescence intensity in MCF-7 spheroid's core (0.25*r*), intermediate layers (0.50*r* and 0.75*r*), and surface (1.00*r*) upon incubation with (A) 20, 40, and 100 nm carboxylate (COOH) particles and (B) anionic (COOH), cationic (NH_2), and neutral (nonfunctionalized) 20 nm particles. Fifty microliters of Optison microbubbles was added to the spheroids' solution without applying the US field. Fluorescence intensity in the surface (1.00*r*) and intermediate layers (0.50*r* and 0.75*r*) is normalized to the fluorescence intensity in the core (0.25*r*) to account for the difference in the intrinsic fluorescence properties of different particles. All results are the average of 15 samples ± the standard error of the mean. The *** indicates $p < 0.005$ when comparing (A) the increase in fluorescence fold for 20 and 40 nm particles to that observed with 100 nm particles and (B) the increase in fluorescence fold for anionic and cationic 20 nm particles to that observed with neutral particles.

the spheroid's core (0.25*r*), intermediate layers (0.50*r* and 0.75*r*), and surface (1.00*r*) after US exposure was compared to the fluorescence intensity observed in control spheroids that were not exposed to US to determine the fold increase in particle penetration into different spheroid layers. We evaluated the intrinsic penetration properties of different particles into MCF-7 spheroids without the application of pulsed US as a function of their size and surface charge by measuring the fluorescence intensity in each layer and normalizing it to the fluorescence intensity in the spheroid's core (0.25*r*) to account for the difference in particle's fluorescence (Figure 4). Results show that anionic carboxylate particles exhibit size-dependent penetration into MCF-7 spheroids where smaller 20 and 40 nm particles show statistically higher (8.5- and 11.1-fold) adhesion and penetration into the spheroid's surface (1.00*r*) compared to larger 100 nm particles (4.4-fold) (Figure 4, panel A). Similarly, the 40 nm carboxylate particles showed higher penetration (5.7-fold) into the 0.75*r* intermediate layer compared to the larger 100 nm particles (2.5-fold). All carboxylate particles (20, 40, and 100 nm) showed similar limited penetration into the deeper intermediate (0.50*r*) and core (0.25*r*) layers of MCF-7 spheroids. Anionic, cationic, and neutral 20 nm particles showed a charge-dependent penetration profile into MCF-7 spheroids (Figure 4, panel B). Anionic and cationic particles exhibited statistically higher (12.7- and 7.4-fold) adhesion and penetration into the spheroid's surface (1.00*r*) compared to neutral particles (3.3-fold). Anionic, cationic, and neutral 20 nm particles showed 5.6-, 3.3-, and 2.2-fold higher penetration into the 0.75*r* intermediate layer compared to the spheroid's core (0.25*r*) following the same charge-dependent penetration profile. All particles irrespective of the surface charge showed low penetration into the deeper intermediate (0.50*r*) and core (0.25*r*) layers of the MCF-7 spheroids.

Effect of US Parameters on Penetration of 100 nm Carboxylate Particles into Breast Cancer Spheroids. Results show that US radiation for 30, 60, and 90 s duration at 10% DC increased the adhesion of 100 nm particles to the spheroids surface (1.00*r*) by 2-, 1.6-, and 3.8-fold compared to the control group, respectively (Figure 5, panel A). US exposure also increased particle penetration into the intermediate layers (0.75*r* and 0.50*r*) by 4- and 2.8-fold for 90 s exposure compared to 2.3- and 2.6-fold increase for 60 s exposure and 1.9- and 1.7-fold increase for 30 s exposure, which indicates that longer exposure times increased particle penetration for the same DC and acoustic pressure. However, there was no significant increase in particle penetration into the spheroid's core (0.25*r*) at this US DC (10%) regardless of the exposure time (Figure 5, panel A).

Increasing the US DC to 20% and 40% appeared to increasingly drive the 100 nm particles from the spheroid surface (1.00*r*) deeper into the core (0.25*r*) (Figure 5, panels B and C). US radiation at 20% DC for 90 s generated a 3.7-fold increase in particle concentration in the core (0.25*r*) compared to untreated spheroids (Figure 5, panel B). US exposure at 20% DC increased particle concentration in the 0.50*r* region by 2.3- to 3.9-fold after 60 and 90 s exposure compared to 1.9- to 2.3-fold increase after 60 and 90 s exposure in the 0.75*r* layer, respectively (Figure 5, panel B). It is noted that particles on the spheroid's surface dropped to 1.5-fold compared to the 3.8-fold observed upon applying US at 10% DC (Figure 5, panel A).

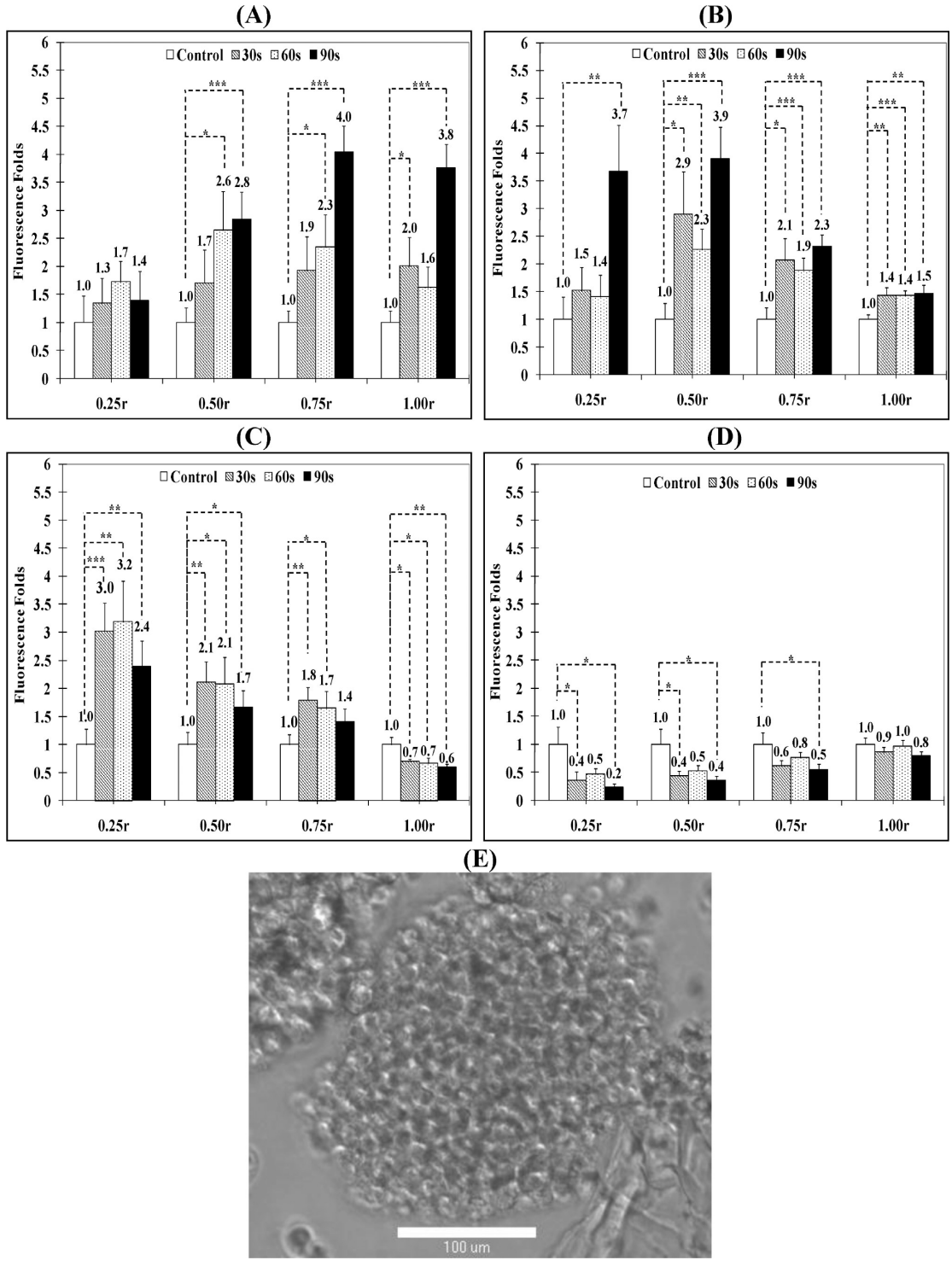

Figure 5. Change in fluorescence intensity in MCF-7 spheroid's core (0.25*r*), intermediate layers (0.50*r* and 0.75*r*), and surface (1.00*r*) by FITC-loaded 100 nm particles with carboxylic acid surface groups after exposure to pulsed US at (A) 10% DC, (B) 20% DC, (C) 40% DC, and (D) 50% DC for different exposure times compared to spheroids that were not exposed to US. Fifty microliters of Optison microbubbles was added to the spheroid solution before US exposure. All results are the average of 15 samples ± the standard error of the mean. The * indicates $p < 0.05$, ** $p < 0.01$, and *** $p < 0.005$ when comparing the test and control groups. (E) A representative phase contrast image of MCF-7 spheroids suspended in PBS, mixed with 100 nm FITC-loaded particles and 50 μL of Optison microspheres, and exposed to US (center frequency 1 MHz, acoustic pressure 0.5 MPa, pulse repition frequency 10 Hz, and duty cycle 50%) for 60 s. The image clearly shows the fragmentation and loss of integrity of the irradiated spheroid.

Maximum penetration of the 100 nm carboxylate particles into the spheroid core (0.25*r*) was observed for US exposure at 40% DC for 30, 60, and 90 s resulting in 3.0-, 3.2-, and 2.4-fold increase in particle concentration compared to control spheroids, respectively (Figure 5, panel C). Similarly, particle concentration in the intermediate layers (0.50*r* and 0.75*r*) increased by 2.1- and 1.7-fold for 60 s exposure coupled with a significant drop in particle adhesion and retention on the spheroid's surface (1.00*r*) (Figure 5, panel C). These results show that increasing the DC of the applied US pulses from 10−40% results in an increase in the penetration of 100 nm carboxylate particles deeper into the MCF-7 spheroids core by 3−4-fold.

US application at 50% DC to MCF-7 spheroids did not produce an increase in particle penetration into the spheroid's core (0.25*r*) but rather reduced particle retention in the spheroid's surface (1.00*r*), intermediate layers (0.75*r* and 0.50*r*), and core (0.25*r*) (Figure 5, panel D). Microscopic examination of the spheroids revealed their fragmentation, loosening of cell packing, and formation of cellular debris at this DC (Figure 5, panel E).

US Enhanced Penetration of 40 nm Carboxylate Particles into Breast Cancer Spheroids. US enhanced penetration of 40 nm carboxylate particles into MCF-7 spheroids is shown in Figure 6. US pulses with 10% DC increased the particle concentration in the spheroid's core (0.25*r*) by 2.8-, 3.4-, and 2.6-fold for 30, 60, and 90 s exposure, but no apparent increase was observed in the intermediate layers and spheroid surface (Figure 6, panel A). US application at 20% DC increased particle concentration in the spheroid's core (0.25*r*) up to 5.9-fold after 60 s of exposure compared to control spheroids (Figure 6, panel B), which is higher than the observed 1.4-fold increase in the penetration of 100 nm carboxylate particles under the same experimental conditions (Figure 5, panel B). However, 90 s exposure produced a comparable increase for the 40 nm particles (3.2-fold) and the 100 nm particles (3.7-fold). Penetration and retention of 40 nm particles into the intermediate layers (0.50*r* and 0.75*r*) also increased by 3.4- and 2.2-fold after 60 s of exposure, and adhesion to the spheroid's surface increased by 2- to 3.5-fold compared to control spheroids for 30 and 90 s exposures (Figure 6, panel B).

Increasing the US duty cycle to 40% resulted in the maximum penetration of 40 nm carboxylate particles into the spheroid's core (0.25*r*) reaching 9.1-fold after 90 s of exposure compared to control spheroids and penetration into the intermediate layers (0.50*r* and 0.75*r*) also increased by 6.6- and 3.4-fold, respectively (Figure 6, panel C). Increasing DC further to 50% increased particle penetration into the spheroid's core (0.25*r*) and intermediate layers (0.50*r* and 0.75*r*) by 2.3-, 2.0-, and 1.5-fold, respectively, after 90 s exposure (Figure 6, panel D). The spheroids exhibited minor fragmentation and swelling at this duty cycle (Figure 6, panel E). These results show that reducing the particle size down to 40 nm increases their penetration into MCF-7 spheroids reaching the maximum concentration in the core (0.25*r*) upon exposure to US at 40% DC.

US Enhanced Penetration of 20 nm Carboxylate Particles into Breast Cancer Spheroids. Penetration of 20 nm particles into MCF-7 spheroids was examined to further illustrate the impact of particle size (Figure 7). At 10% DC, particle penetration into the spheroid's core (0.25*r*) increased by 2.3-, 3.7-, and 4.7-fold after 30, 60, and 90 s exposure (Figure 7, panel A). Similarly, penetration into the intermediate layers (0.50*r* and 0.75*r*) increased by 2.2- to 4.1-fold while particle adhesion to the spheroid's surface (1.00*r*) was 1.6- to 2.0-fold higher than the control with increasing exposure durations from 30 to 90 s (Figure 7, panel A). Maximum penetration of 20 nm particles into MCF-7 spheroids was observed with US pulse at 30% DC. Particle penetration into the spheroid's core (0.25*r*) was 3.5- and 6.0-fold higher than control spheroids after 30 and 90 s US exposure, respectively (Figure 7, panel C). In addition, penetration in the intermediate layers (0.50*r* and 0.75*r*) increased by 15.6- and 20.4-fold after 90 s exposure while particle adhesion onto the spheroid's surface (1.00*r*) increased by 3.6- to 10.0-fold after 30 and 90 s exposure (Figure 7, panel C). Further, increasing the duty cycle of the applied US pulse to 40% maintained particle penetration into the spheroid's core at 1.2- to 4.7-fold higher than the control group after 30 and 90 s exposure (Figure 7, panel D). Similarly, particle penetration into the intermediate layers (0.50*r* and 0.75*r*) was 9.9- and 8.5-fold whereas particle adhesion to spheroid's surface was 3.3-fold higher than control spheroids after 90 s exposure (Figure 7, panel D). A similar trend was observed for US pulses at 50% DC with no visible evidence of spheroids fragmentation or swelling (Figure 7, panel E).

Effect of Surface Charge on Particle Penetration into Breast Cancer Spheroids. Surface charge of polymer and lipid particles has been shown to influence their *in vivo* distribution,[78] interaction with epithelial[79−81] and endothelial barriers,[82] and uptake into cancer cells.[83,84] Cationic polymers are routinely used to complex and deliver therapeutic nucleic acids into a wide range of cancer cells due to their efficient internalization by target cells.[85] Anionic magnetic particles also

(78) He, C.; Hu, Y.; Yin, L.; Tang, C.; Yin, C. Effects of particle size and surface charge on cellular uptake and biodistribution of polymeric nanoparticles. *Biomaterials* **2010**, *31* (13), 3657–3666.

(79) Tajarobi, F.; El-Sayed, M.; Rege, B.; Polli, J.; Ghandehari, H. Transepithelial transport of poly (amidoamine) (PAMAM) dendrimers across Madin-Darby Canine Kidney (MDCK) cells. *Int. J. Pharm.* **2001**, *215* (1−2), 263–267.

(80) El-Sayed, M.; Ginski, M.; Rhodes, C.; Ghandehari, H. Transepithelial transport of poly (amidoamine) dendrimers across Caco-2 cell monolayers. *J. Controlled Release* **2002**, *81* (3), 355–365.

(81) El-Sayed, M.; Ginski, M.; Rhodes, C.; Ghandehari, H. Influence of surface chemistry of poly (amidoamine) dendrimers on Caco-2 cell monolayers. *J. Bioact. Compat. Polym.* **2003**, *18* (1), 7–22.

(82) El-Sayed, M.; Kiani, M. F.; Naimark, M. D.; Hikal, A. H.; Ghandehari, H. Extravasation of poly (amidoamine) (PAMAM) dendrimers across microvascular network endothelium. *Pharm. Res.* **2001**, *18* (1), 23–28.

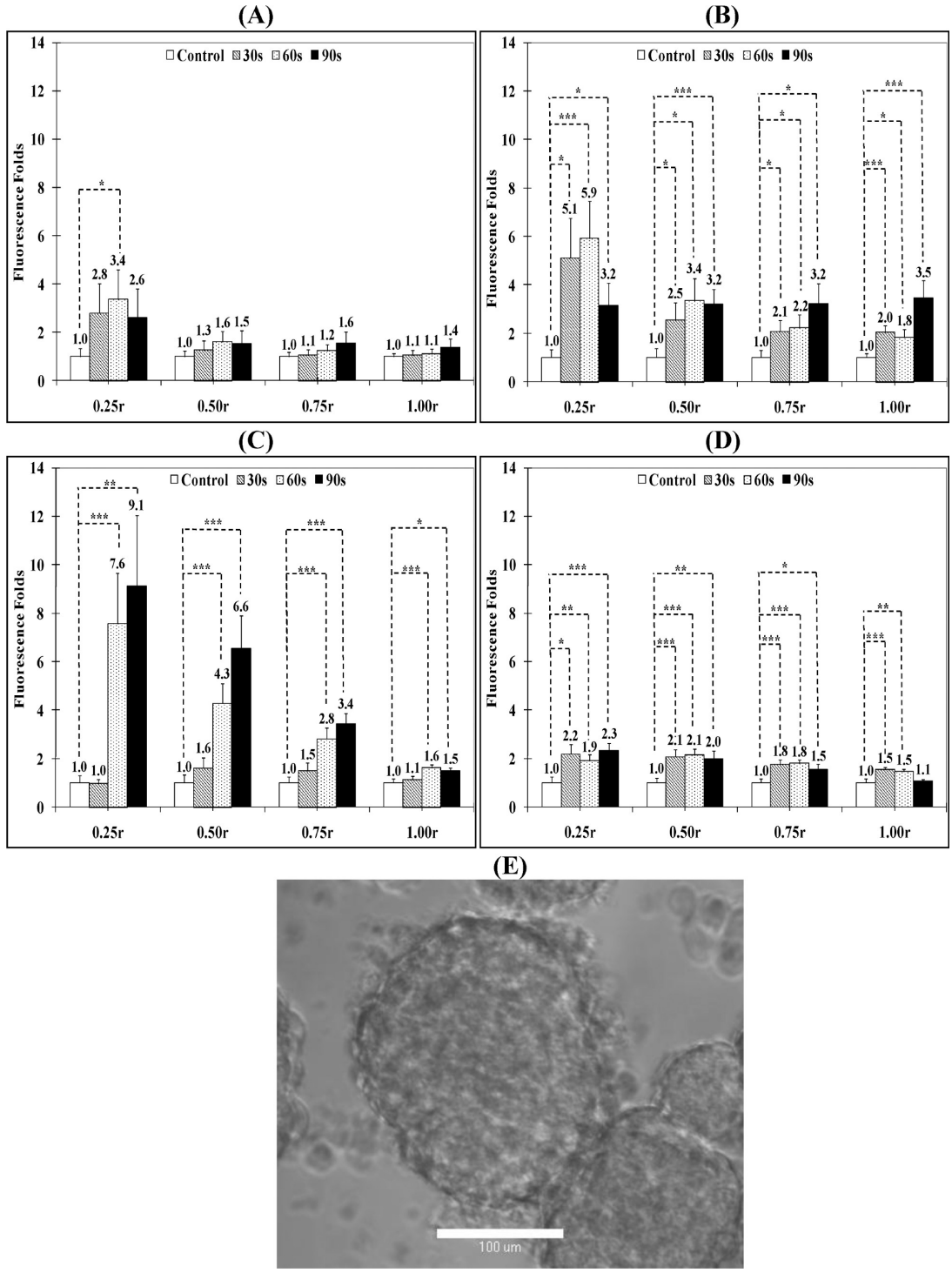

Figure 6. Change in fluorescence intensity in the core (0.25*r*), intermediate layers (0.50*r* and 0.75*r*), and surface (1.00*r*) of MCF-7 spheroids by FITC-loaded 40 nm particles with carboxylic acid surface groups and exposed to pulsed US at (A) 10% DC, (B) 20% DC, (C) 40% DC, and (D) 50% DC compared to spheroids that were not exposed to US. Fifty microliters of Optison microbubbles was added to the spheroid solution before US exposure. All results are the average of 15 samples ± the standard error of the mean. The * indicates $p < 0.05$, ** $p < 0.01$, and *** $p < 0.005$ when comparing the test and control groups. (E) A representative phase contrast image of MCF-7 spheroids suspended in PBS, mixed with 40 nm FITC-loaded particles and 50 μL of Optison microspheres, and exposed to US (center frequency 1 MHz, acoustic pressure 0.5 MPa, pulse repition frequency 10 Hz, and duty cycle 50%) for 60 s. The image shows minor fragmentation of the irradiated spheroids.

proved effective in labeling adult, progenitor, immune, and tumor cells.[86−88] Consequently, 20 nm carboxylate- and amine-functionalized polystyrene beads and nonfunctionalized CdSe quantum dots were used in this study to examine the effect of

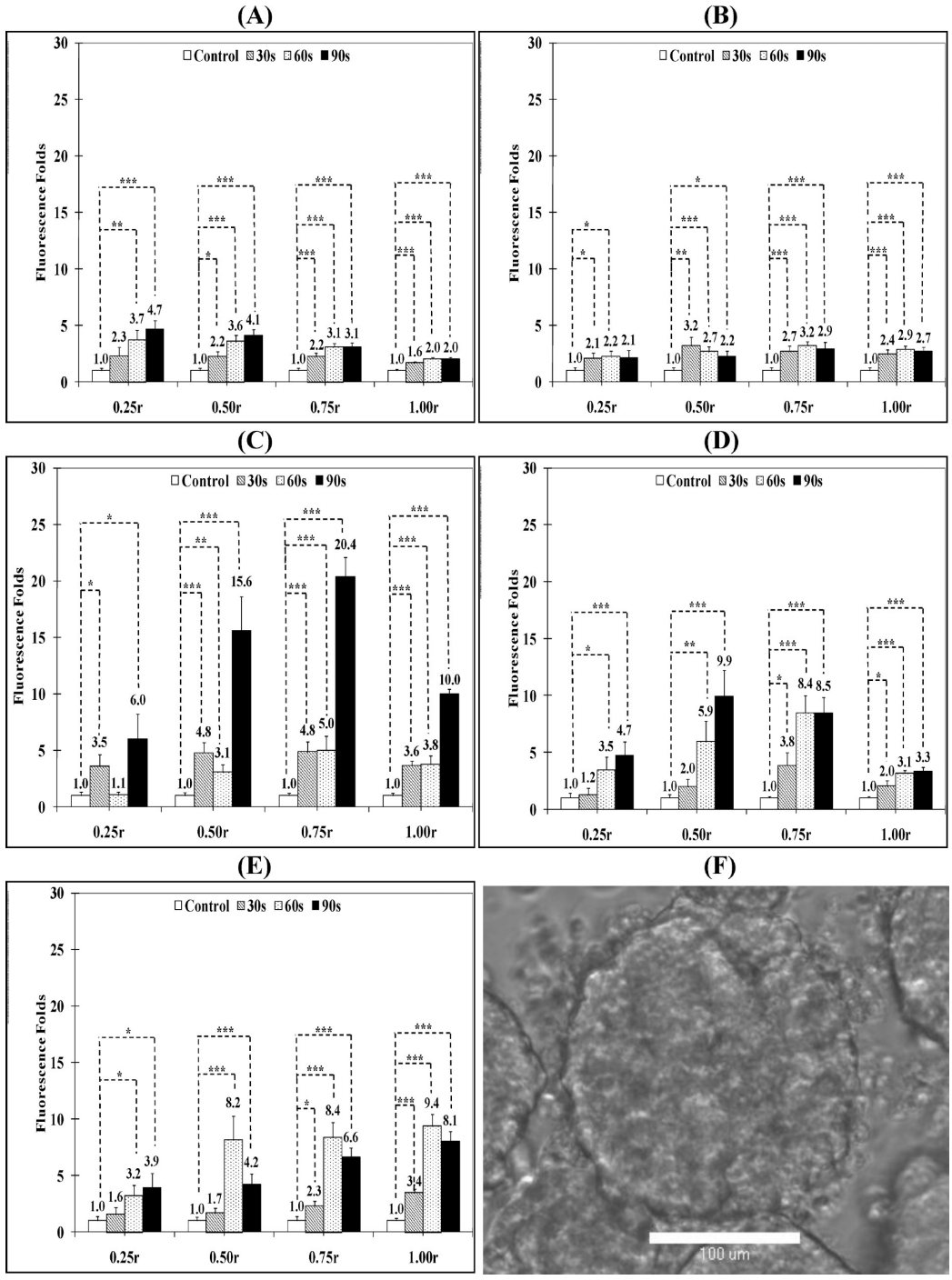

Figure 7. Change in fluorescence intensity in the core (0.25*r*), intermediate layers (0.50*r* and 0.75*r*), and surface (1.00*r*) of MCF-7 spheroids by FITC-loaded 20 nm particles with carboxylic acid surface groups exposed to pulsed US at (A) 10% DC, (B) 20% DC, (C) 30% DC, (D) 40% DC, and (E) 50% DC compared to spheroids that were not exposed to US. Fifty microliters of Optison microbubbles was added to the spheroid solution before US exposure. All results are the average of 15 samples ± the standard error of the mean. The * indicates $p < 0.05$, ** $p < 0.01$, and *** $p < 0.005$ when comparing the test and control groups. (F) A representative phase contrast image of MCF-7 spheroids suspended in PBS, mixed with 20 nm FITC-loaded particles and 50 μL of Optison microspheres, and exposed to US (center frequency 1 MHz, acoustic pressure 0.5 MPa, pulse repition frequency 10 Hz, and duty cycle 50%) for 60 s. The image shows no fragmentation or swelling of the irradiated spheroids.

anionic, cationic, and neutral surface charges on particle penetration into MCF-7 spheroids. The penetration of cationic and neutral 20 nm particles into MCF-7 spheroids exposed to pulsed US at 10% DC was evaluated to eliminate the contribution of particle size and possible fragmentation of the spheroids to the observed results (Figure 8). US pulses at 10% DC resulted in similar increase in penetration of neutral CdSe (2.2-, 1.9-, and 2.4-fold after 30, 60, and 90 s exposure) and cationic amine-functionalized (1.5-, 1.4-, and 1.9-fold) particles into the spheroid's core (0.25*r*) compared to control spheroids (Figure

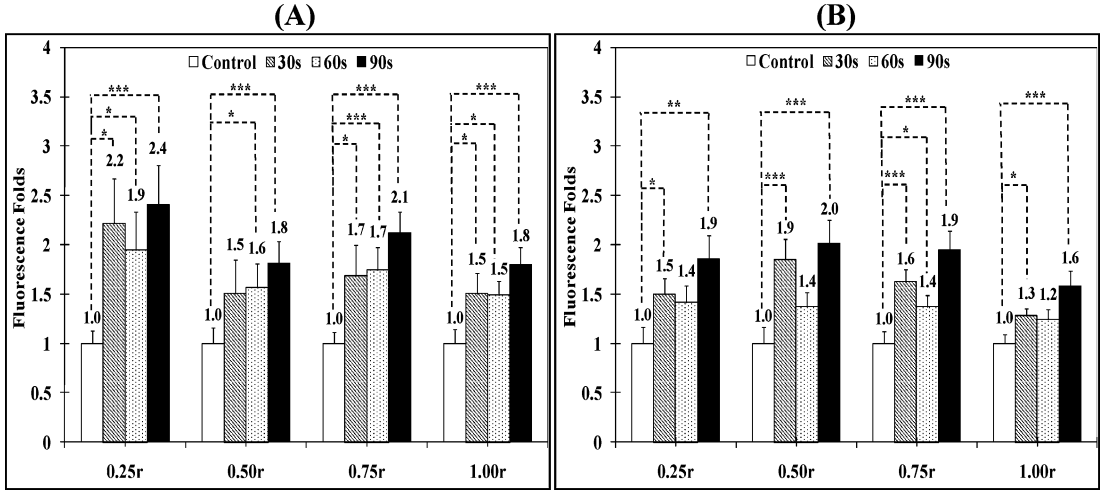

Figure 8. Change in fluorescence intensity in MCF-7 spheroid's core (0.25*r*), intermediate layers (0.50*r* and 0.75*r*), and surface (1.00*r*) upon incubation with 50 μL of Optison microspheres and (A) 20 nm CdSe particles with nonfunctionalized surface (neutral) or (B) 20 nm cationic particles with primary amine surface groups upon exposure to pulsed US at 10% DC. All results are the average of 15 samples $\pm$ the standard error of the mean. The * indicates $p < 0.05$, ** $p < 0.01$, and *** $p < 0.005$ when comparing the test and control groups.

8). Neutral and cationic particles also exhibited similar increased penetration (neutral particles: 1.5-, 1.6-, and 1.8-fold in 0.50*r* layer and 1.7-, 1.7-, and 2.1-fold in 0.75*r* layer) (cationic particles: 1.9-, 1.4-, and 2.0-fold in 0.50*r* layer and 1.6-, 1.4-, and 1.9-fold in 0.75*r* layer) into the spheroid's intermediate layers (0.50*r* and 0.75*r*) and adhesion to the surface (1.00*r*) (neutral particles: 1.5-, 1.5-, and 1.8-fold and cationic particles: 1.3-, 1.2-, and 1.6-fold) compared to control spheroids (Figure 8).

Discussion

This study examines the effect of DC of pulsed US on the penetration of nanoparticles of different size and surface chemistry/charge into a 3D model of cultured breast cancer cells. The use of pulsed US, rather than a single tone burst US exposure, is to generate dynamic fluid flow without causing cell death for a sustained period of time. While the mechanical effects generated by pulsed US exposures are affected by all the US parameters, including the acoustic pressure, PRF, and DC, in a related and complex way, this study focused on the effects of US DC with a fixed acoustic pressure (0.5 MPa and PRF of 10 Hz) to illustrate the enhancement of particle penetration in a 3D volume of cells by pulsed US exposures. Based on a preliminary experimental investigation, the US parameters used in this study were chosen to generate sufficient enhancement and to preserve cell viability and spheroid integrity. Concentration of the microbubbles used in this study was $\sim 25 \times 10^6$ bubbles/mL. Although experiments were done consistently with this condition, floating of the microbubbles could effectively reduce the bubble concentration surrounding the spheroids and may induce variability in experimental results.

This study utilized viable MCF-7 breast cancer cell spheroids with a diameter of ~ 350 μm, which, despite being much smaller in volume and lacking the vascular and lymphatic networks present *in vivo* in solid tumors, still provide a spherical volume with three-dimensional (3D) arrangements of breast cancer cells with tight cell-to-cell contact[89,90] and extracellular matrix similar to those present in tumor tissue[91,92] that play critical roles in particle transport in solid tumors.

(83) Campbell, R. B.; Fukumura, D.; Brown, E. B.; Mazzola, L. M.; Izumi, Y.; Jain, R. K.; Torchilin, V. P.; Munn, L. L. Cationic charge determines the distribution of liposomes between the vascular and extravascular compartments of tumors. *Cancer Res.* **2002**, *62* (23), 6831–6836.

(84) Schluep, T.; Hwang, J.; Hildebrandt, I. J.; Czernin, J.; Choi, C. H. J.; Alabi, C. A.; Mack, B. C.; Davis, M. E. Pharmacokinetics and tumor dynamics of the nanoparticle IT-101 from PET imaging and tumor histological measurements. *Proc. Natl. Acad. Sci. U.S.A.* **2009**, *106* (27), 11394–11399.

(85) Han, S.-E.; Kang, H.; Shim, G. Y.; Kim, S. J.; Choi, H.-G.; Kim, J.; Hahn, S. K.; Oh, Y.-K. Cationic derivatives of biocompatible hyaluronic acids for delivery of siRNA and antisense oligonucleotides. *J. Drug Targeting* **2009**, *17* (2), 123–132.

(86) Wilhelm, C.; Gazeau, F. Universal cell labeling with anionic magnetic nanoparticles. *Biomaterials* **2008**, *29* (22), 3161–3174.

(87) Wilhelm, C.; Billotey, C.; Roger, J.; Pons, J. N.; Bacri, J.-C.; Gazeau, F. Intracellular uptake of anionic superparamagnetic nanoparticles as a function of their surface coating. *Biomaterials* **2003**, *24* (6), 1001–1011.

(88) Wilhelm, C.; Gazeau, F.; Roger, J.; Pons, J. N.; Bacri, J.-C. Interaction of anionic superparamagnetic nanoparticles with cells: kinetic analyses of membrane adsorption and subsequent internalization. *Langmuir* **2002**, *18* (21), 8148–8155.

(89) Ivascu, A.; Kubbies, M. Diversity of cell-mediated adhesions in breast cancer spheroids. *Int. J. Oncol.* **2007**, *31* (6), 1403–1413.

(90) Grantab, R.; Sivananthan, S.; Tannock, I. F. The penetration of anticancer drugs through tumor tissue as a function of cellular adhesion and packing density of tumor cells. *Cancer Res.* **2006**, *66* (2), 1033–1039.

Interplay of DC of Pulsed US Exposures and Particle Size. Results obtained from this study clearly indicate that particle penetration into MCF-7 spheroids depends on particle size. Without the application of pulsed US, smaller 20 and 40 nm particles exhibited high adhesion and penetration into the spheroid's surface (1.00*r*) and intermediate layer (0.75*r*) compared to deeper (0.50*r* and 0.25*r*) layers. Application of pulsed US increased particle penetration into the spheroid's core (0.25) in a size-dependent fashion. Specifically, 20 nm carboxylate particles achieve maximal penetration into MCF-7 spheroids upon exposure to US pulses at 30% DC reaching 6-, 15.6-, 20.4-, and 10-fold higher concentration into the spheroid's core (0.25*r*), intermediate layers (0.50*r* and 0.75*r*), and surface (1.00*r*) compared to control spheroids, respectively. Increasing particle size to 40 nm reduced their net penetration and retention into MCF spheroids to 9.1- (0.25*r*), 6.6- (0.50*r*), 3.4- (0.75*r*), and 1.5-fold (1.00*r*) compared to control spheroids upon exposure to microbubble-enhanced pulsed US at 40% DC. Increasing particle size to 100 nm further reduced their penetration into the spheroids to 3.2- (core; 0.25*r*), 2.1- (0.50*r*), 1.8-fold (0.75*r*) compared to control spheroids upon exposure to microbubble-enhanced US at 40% DC with minimal retention of the fluorescent particles on the spheroids surface (1.00*r*). These results suggest that US enhanced penetration of carboxylate particles into tumor spheroids depends on US DC and 30% DC appears to be optimal to achieve the highest penetration of 20 nm carboxylate particles into tumor spheroids under the current experimental conditions (US pressure of 0.5 MPa, PRF of 10 Hz).

Nanoparticles Transport Driven by Pulsed US Exposures and Facilitated by Microbubbles. Driven by the oscillatory positive and negative pressures of an US field, a gas-filled microbubble undergoes rapid cyclic volume changes and collapse generating significant dynamic activities such as bulk fluid movement and local fluid microstreaming, shear stress, and high speed fluid microjet. These mechanical effects, particularly the significant mechanical impacts from the fluid microjet on a nearby cell causing disruption of the cell membrane (sonoporation),[93−98] have been well recognized and exploited for delivery of otherwise impermeable therapeutic agents into the cell cytoplasm. However, the US-generated mechanical and fluid dynamic effects, in the presence of microbubbles, on the movement of nanoparticles in the medium have not been specifically described in the context of particle transport into a 3D tissue structure.

In this study, the spheriods were in a fluid environment surrounded by microbubbles, which simulate a tissue volume adjacent to a vascular compartment. It is expected that the microbubbles in the fluid, when exposed to pulsed US, will generate the dynamic fluid streaming of different spatial scales (bulk flow and microstreaming near the bubble/cell) and other mechanical effects. Fluid microjets produced by rapid collapse of a bubble can generate sonoporation leading to enhanced intracellular uptake but this likely to be limited to the outmost layer of the cells of the spheroids. Instead, the US generated fluid flow and activities will increase the convective transport of particles suspended in the fluid toward the inner areas of the spheroids. The particles were not in the cytoplasm of the cells deep inside the spheroids. Instead, they were found in the extracellular matrix within the spheroids, which was not in direct contact with the microbubbles. Our results show that the penetration of the particles into the spheroids depends on the mass or size of the particles, which were presumably carried by the fluid flow with smaller particles having deeper penetration (Figures 5−7). Such dependence represents an aspect of the kinetic characteristics of the fluid−particle interaction as a mechanism for the enhanced transport in a 3D cell volume.

In the meantime, the mechanical impacts of the transient yet rapid fluid flow plus those from the movement of the nanoparticles themselves could generate other physical effects on the spheroids. For example, our results show that US application at high 50% DC in the presence of large 100 nm particles resulted in fragmentation, loosening of cell packing, and formation of cellular debris of the spheroids (Figure 5, panel E). The spheroids were much less affected with smaller particles (Figure 7, panel F).

The effects of DC on particles' penetration into the spheroids are illustrated experimentally in this study. Since the enhanced penetration of particles is believed to result from the increased convective transport by the US-generated transient fluid flow/streaming, the effects of DC are then primarily related to the ability of US exposures to generate optimal fluid flow patterns for the particles and spheroids in the configuration (fluid volume, geometry, microbubble concentration, etc.) used in this study. However, exact details of the fluid flow patterns and their interaction with the nanoparticles need to be investigated in future studies.

(91) Sutherland, R. M. Cell and environment interactions in tumor microregions - the multicell spheroid model. *Science* **1988**, *240*, 177–184.
(92) Takagi, A.; Watanabe, M.; Ishii, Y.; Morita, J.; Hirokawa, Y.; Matsuzaki, T.; Shiraishi, T. Three-dimensional cellular spheroid formation provides human prostate tumor cells with tissue-like features. *Anticancer Res.* **2007**, *27* (1A), 45–54.
(93) Prentice, P.; Cuschieri, A.; Dholakia, K.; Prausnitz, M.; Campbell, P. Membrane disruption by optically controlled microbubble cavitation. *Nat. Phys.* **2005**, *1* (2), 107–110.
(94) van Wamel, A.; Kooimana, K.; Hartevelda, M.; Emmera, M.; ten Catec, F. J.; Versluisd, M.; de Jonga, N. Vibrating microbubbles poking individual cells: Drug transfer into cells via sonoporation. *J. Controlled Release* **2006**, *112* (2), 149–155.
(95) Postema, M.; van Wamel, A.; Lanc, C. T.; de Jong, N. Ultrasound-induced encapsulated microbubble phenomena. *Ultrasound Med. Biol.* **2004**, *30* (6), 827–840.
(96) Ohl, C.-D.; Arora, M.; Ikink, R.; de Jong, N.; Versluis, M.; Delius, M.; Lohse, D. Sonoporation from jetting cavitation bubbles. *Biophys. J.* **2006**, *91* (11), 4285–4295.
(97) Wu, J. Shear stress in cells generated by ultrasound. *Prog. Biophys. Mol. Biol.* **2007**, *93* (1−3), 363–373.
(98) VanBavel, E. Effects of shear stress on endothelial cells: Possible relevance for ultrasound applications. *Prog. Biophys. Mol. Biol.* **2007**, *93* (1−3), 374–383.

Effect of Particle Charge. From a comparison of the penetration profile of neutral and cationic particles to that observed with 20 nm carboxylate particles, it is clear that concentration of the anionic particles in the spheroid core (0.25*r*), intermediate layers (0.50*r* and 0.75*r*) and surface (1.00*r*) is almost twice as much (Figure 7, panel A) as the concentration of neutral and cationic particles (Figure 8). This is consistent with earlier reports that showed that anionic dextran moves with a higher average velocity through the interstitium than neutral molecules with similar size due to the electrostatic repulsion with the negatively charged residues present in the extracellular matrix holding the cancer cells.[99,100] These results suggest that, even with pulsed US application, small anionic nanoparticles might be better suited as carriers for penetration and retention into tumor tissue although microbubble-facilitated pulsed US application is also capable of increasing the penetration of neutral and cationic particles into the deeper layers of breast cancer spheroids.

Conclusions

Results from this study demonstrate that nanoparticle penetration into the core of 3D tumor spheroids can be enhanced by pulsed US exposures in the presence of microbubbles. Concentration of particles in the spheroid's core (0.25*r*) and intermediate layers (0.50*r* and 0.75*r*) and near the surface (1.00*r*) depends on particle size, surface charge, and DC of the applied US field. Specifically, penetration into MCF-7 spheroids decreases with increasing particle size. Maximum penetration into the spheroid's core was observed with 20 nm carboxylate particles. In addition, anionic carboxylate particles exhibited the highest penetration into the tumor's core compared to neutral and cationic particles under the same experimental conditions. These studies provide evidence that microbubble-enhanced pulsed US application can serve as a synergistic tool to increase the penetration and effective concentration of therapeutic and diagnostic nanoparticles into solid tumors.

Acknowledgment. This research is supported by the Department of Defense Breast Cancer Research Program (W81XWH-05-1-0240; M.E.H.E.) and the National Institutes of Health (R01CA116592; C.X.D.). S.J.G. acknowledges the financial support of the University of Michigan Rackham Merit Fellowship and the University of Michigan Cellular Biotechnology Training Program. We thank Dr. Michael Mayer for providing access to the Nikon EZ-C1 3.50 confocal microscope used in these studies.

MP100280B

(99) Aukland, K.; Reed, R. K. Interstitial-lymphatic mechanisms in the control of extracellular fluid volume. *Physiol. Rev.* **1993**, *73*, 1–78.

(100) Reddy, S. T.; Berk, D. A.; Jain, R. K.; Swartz, M. A. A sensitive *in vivo* model for quantifying interstitial convective transport of injected macromolecules and nanoparticles. *J. Appl. Physiol.* **2006**, *101*, 1162–1169.